Journal of Materials Chemistry A

ROYAL SOCIETY OF CHEMISTRY

PAPER

View Article Online
View Journal | View Issue

Cite this: J. Mater. Chem. A, 2020, 8, 11011

Tailored nanoscale interface in a hierarchical carbon nanotube supported MoS_2@MoO_2-C electrode toward high performance sodium ion storage†

Chunrong Ma, [ab] Zhixin Xu,[c] Jiali Jiang,[a] ZiFeng Ma, [c] Tristan Olsen,[b] Hui Xiong, *[b] Shuguang Wang*[a] and Xian-Zheng Yuan *[a]

Received 26th March 2020
Accepted 10th May 2020

DOI: 10.1039/d0ta03390a

rsc.li/materials-a

Tailoring heterointerfaces at atomic and molecular levels in electrode materials for superior structural stability and enhanced power/energy densities is desired yet still challenging for achieving ultrafast and stable Na-ion batteries. Herein, an MoS_2/MoO_2 heterointerface is designed and created, in which ultrafine MoO_2 nanocrystals are tightly anchored on ultrathin MoS_2 nanosheets, with the assistance of an N-doped carbon protecting layer, on flexible carbon nanotubes. The electrode exhibits a high specific capacity of ~700 mA h g^{-1} at 0.2 A g^{-1} and an ultra-long cycling stability over 6000 cycles at 5 A g^{-1}. Moreover, an excellent rate capability of ~375 mA h g^{-1} at 10 A g^{-1} is retained. As evidenced by both experiments and density functional theory (DFT) calculations, the heterointerface could not only introduce an electric field to reduce the charge transport barrier, but also provide extra active sites to adsorb Na^+. Meanwhile, within the designed nanoarchitecture, the MoO_2 nanocrystals can effectively reduce the aggregation of MoS_2 during charge/discharge processes, and adsorb polysulfide to improve the reversibility. This work provides a fundamental understanding of engineering heterointerfaces at the atomic level for enhanced Na^+ storage and transport, which can be extended to other functional electrode materials.

Introduction

In the past decades, lithium ion batteries (LIBs) as the energy storage system have been widely applied in portable electronic products, electric vehicles, and grid-scale energy storage. With the market demand growth, the limited lithium resource and uneven distribution cannot meet the large-scale application.[1–3] Considering the electrochemical similarity between lithium and sodium, sodium ion batteries (SIBs) as one of the most promising candidates aroused extensive attention due to the abundance of the sodium resource in the Earth's crust. However, the ionic radius of Na^+ is larger than that of Li^+, which leads to sluggish reaction kinetics, severe structural collapse of the active material, and an unstable solid electrolyte interphase (SEI), these eventually give rise to inferior electrochemical performance.[4,5] Therefore, exploring a suitable anode material is the key point to enhance the Na^+ storage for SIBs. Among the anode materials, MoS_2 has been extensively investigated because of its high theoretical specific capacity, and unique two-dimensional structure with large interlayer spacing.[6–8] Despite these merits, the application of MoS_2 is still limited by the poor intrinsic conductivity, and structural pulverization with the conversion reaction. Therefore, it is particularly important to rationally design a robust and enhanced structure to promote the reaction kinetics and buffer the volume change simultaneously.

Nanoarchitecturing through robust nano-carbon scaffolds has been considered as an effective way to reduce the ion diffusion path and relieve volume expansion during cycling.[9–14] Based on such considerations, different MoS_2–carbon composites were explored to improve the cyclability of SIBs, such as MoS_2/graphene, MoS_2/carbon spheres, MoS_2/carbon nanotubes, and MoS_2/carbon networks.[15–19] Although progress has been made, challenges still remain for the practical application of MoS_2 in SIBs. Self-aggregation is inevitable during repeated charge/discharge processes because of the weak bonding force between MoS_2 and the carbon matrix, leading to the burial of active sites.[20] Furthermore, the polysulfides generated from the conversion reaction during the discharge

[a]Shandong Key Laboratory of Water Pollution Control and Resource Reuse, School of Environmental Science and Engineering, Shandong University, Qingdao, 266237, China. E-mail: xzyuan@sdu.edu.cn

[b]Micron School of Materials Science and Engineering, Boise State University, Boise, ID 83725, USA

[c]Shanghai Electrochemical Energy Devices Research Centre, School of Chemistry and Chemical Engineering, Shanghai Jiao Tong University, Shanghai, 200240, China

† Electronic supplementary information (ESI) available. See DOI: 10.1039/d0ta03390a

process could bring severe redox shuttle issues and lead to irreversible capacity loss.[8] Recently, heterointerfaces have attracted great attention ranging from optoelectronic devices to electronic instruments, which can afford unprecedented properties by accelerating the charge separation and offering more active sites. For instance, MoS_2/TiO_2,[21] SnS/SnO_2,[22] Sb_2S_3/SnS_2,[23] TiO_2/MoO_2 (ref. 24) and Co_9S_8/ZnS (ref. 25) heterostructures have demonstrated higher specific capacity, enhanced electron mobility and superior rate capability. Nevertheless, the reported heterostructures tend to form dendritic/dumbbell-like morphology owing to the lattice mismatch between different crystal structures, which leads to undesirable structural instability and poor cycling life. Meanwhile, the interfacial bonding within the heterointerface is crucial to the understanding of the Na^+ storage mechanism in the composites. Thereby, it is urgent to explore new strategies to realize the controllable synthesis of stable heterointerfaces and provide more insights regarding the mechanisms of their synergistic effect.

Based on first-principle calculations, nano-heterointerfaces can effectively improve the structural stability of electrode materials by providing a stronger interface and larger contact area, enabling faster electron transfer.[15] Meanwhile, defects formed between the interfaces could provide an additional pseudocapacitive contribution.[8] Using this as an inspiration, we designed a MoS_2/MoO_2 hybrid with an ideal nano-heterointerface, in which few-layer MoS_2 and MoO_2 nanocrystals are sandwiched by N-doped carbon anchoring on a carbon nanotube (CNT) surface (CNT-MoS_2@MoO_2-C). This system could provide solutions to the stability challenges associated with MoS_2-based negative electrodes for SIBs. In this structure, MoO_2 nanocrystals are well distributed within MoS_2 nanosheets to avoid the aggregation of MoS_2 during charge/discharge processes, as well as to adsorb polysulfides to improve the reversibility. Moreover, the nano-interface between MoS_2 and MoO_2 crystals, compared to the traditional limited interfacial contact, could provide additional sites for charge storage and promote electron and ion transport. Furthermore, the N-doped carbon can facilitate fast ion diffusion, and act as the protection shell to strengthen the structural durability of the nanocomposite simultaneously. Consequently, the prepared CNT-MoS_2@MoO_2-C electrode exhibited a high reversible capacity of ~375 mA h g^{-1} at 10 A g^{-1} and excellent cycling stability (stable over 6000 cycles at 5 A g^{-1}). Galvanostatic intermittence titration techniques (GITTs) and density-functional theory (DFT) calculations were performed to provide in-depth insights on the interfacial charge storage and transport mechanism. Such a synergistic design strategy may open a new avenue for the rational design of hierarchical nanostructured electrode materials as well as unveil the role of the interface in hierarchical nanocomposites for high performance SIBs.

Results and discussion

The synthesis process of CNT-MoS_2@MoO_2-C is illustrated in Scheme 1. The CNT-MoS_2 composite was first synthesized by a hydrothermal method. Subsequently, the MoO_2 nanocrystals were formed on the MoS_2 nanosheets *via* self-polymerization of dopamine with $Mo_7O_{24}^{6-}$ under alkaline conditions. Finally, CNT-MoS_2@MoO_2-C was obtained by thermal treatment under an Ar atmosphere. The morphology and structural features were characterized using scanning electron microscopy (SEM) and transmission electron microscopy (TEM). As shown in Fig. 1a, the 1D structure of the prepared CNT-MoS_2 is preserved and has a coarse surface, which is uniformly covered by densely packed and wrinkled MoS_2 nanosheets, and the diameter of the prepared CNT-MoS_2 is ~300 nm. Fig. 1b shows that the CNT-MoS_2@MoO_2-C maintains the 1D structure after introducing MoO_2 nanocrystals. SEM (Fig. 1c) distinctly shows that numerous plate-like structures are vertically aligned on the surface of carbon with a thickness of ~13 nm. From the high-magnification image (Fig. 1c inset), voids enclosed by the sheet-structure form at the surface. This porous structure can not only effectively accommodate volume change during repeated charge/discharge processes, but also increase the specific surface area. Fig. 1d shows the typical TEM image of CNT-MoS_2@MoO_2-C, where the 1D CNTs are uniformly coated by the 2D structure, indicating that 2D MoS_2 nanosheets with a folded structure have been successfully grown on the CNT surface. The TEM image of individual 2D sheets is illustrated in

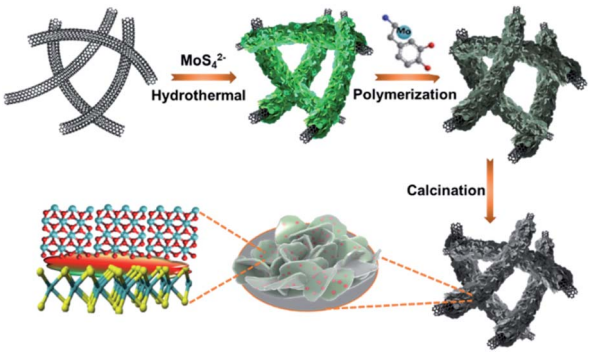

Scheme 1 Schematic illustration of the preparation of CNT-MoS_2@-MoO_2-C.

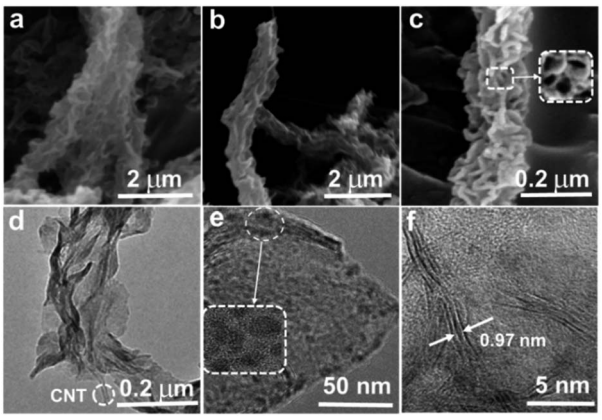

Fig. 1 (a) SEM image of CNT-MoS_2, (b–f) SEM, TEM and high resolution TEM images of CNT-MoS_2@MoO_2-C.

Fig. 1e revealing that the MoO_2 nanocrystals are successfully distributed on the surface of MoS_2 sheets without aggregation. To further demonstrate the characteristics of MoO_2 nanocrystals, the high-resolution TEM image (Fig. 1e inset) shows that the nanocrystals are clearly visible with the size of ~3 nm on the surface of MoS_2 nanosheets. The excellent distribution of MoO_2 nanocrystals can be attributed to the polymerization of dopamine together with MoO_4^{2-}. Dopamine contains a rich catechol group that has the ability to chelate and adsorb a variety of metal ions during self-polymerization, which would react with the Mo–S group to ensure that the MoO_2 crystals can effectively grow on the surface of MoS_2.[26] Meanwhile, the nanocrystals that are uniformly embedded in the carbon matrix form a robust shell, which could reduce aggregation of nanocrystals and restrict nanocrystal growth during the thermal treatment. The few-layered structure with an interlayer distance of 0.96 nm is shown in Fig. 1f, which can be ascribed to the (002) lattice plane of MoS_2, indicating the expanded layer feature. To further confirm the successful attachment of MoO_2 nanocrystals on MoS_2 nanosheets, the TEM images of CNT-MoS_2 are detected (as shown in Fig. S1a and b†). Bare CNT-MoS_2 obtained by the same experimental procedure without MoO_2-C shows a smooth surface, no nanocrystals can be seen. When MoO_2 nanocrystals are introduced on the MoS_2 nanosheets, the surface is obviously dotted with well-dispersed nanocrystals (Fig. S1c and d†). MoS_2 and MoO_2 are combined closely under the effect of van der Waals forces near the boundary.[27] In addition, the carbon-induced by the dopamine could strengthen the structural durability of the heterojunction simultaneously.

The structure of the as-prepared CNT-MoS_2@MoO_2-C was further investigated by XRD. In the XRD pattern (Fig. 2a), a broad peak can be seen at $2\theta = 26.5°$, which can be attributed to the amorphous MoO_2. All the other diffraction peaks match well with the hexagonal MoS_2 (JCPDS card no. 37-1492). Notably, the (002) peak related to the crystal structure of multilayer MoS_2 is not detected, but a sharp peak at 8.9° (1*) and a wide peak at 17.4° (2*) appear, which can be attributed to the few-layer MoS_2 nanosheets.[15,18,28] According to Bragg's law ($2d \sin\theta = n\lambda$),[29] the calculated interlayer spacing of the peak (1*) is 0.97 nm, which agrees with the TEM results. Raman spectroscopy was carried out to elucidate the crystal structure and composition of the as-prepared nanocomposite. In Fig. 2b, there are two distinct peaks located at 1335 and 1574 cm^{-1} for both CNT-MoS_2@MoO_2-C and CNT-MoS_2, representing the D (disorder) and G bands (graphitic) of carbon, respectively. Compared to the I_D/I_G of CNT-MoS_2 (0.98), CNT-MoS_2@MoO_2-C shows a higher I_D/I_G (1.17) due to the larger number of defects caused by the N-doped carbon. As shown in Fig. S2† peaks at round 380 and 401 cm^{-1} are detected, which correspond to the in-plane E^1_{2g} mode and out-of-plane A_{1g} mode of MoS_2, respectively.[30] The remaining peaks located at 191, 387, 317, and 664 cm^{-1} are the characteristic peaks of MoO_2, demonstrating the successful introduction of MoO_2 on the MoS_2 surface.[31] Thermogravimetric analysis (TGA) was performed to examine the carbon content in the CNT-MoS_2@MoO_2-C composite. According to the literature,[32] MoS_2 can be oxidized to MoO_3 in air, then the pure MoS_2@MoO_2 was also examined for the purpose of quantitative analysis. In comparison with the 13.8% weight loss of pure MoS_2, CNT-MoS_2 and CNT-MoS_2@MoO_2-C demonstrate 27.6 and 31.2% weight loss, the calculated content of MoS_2@MoO_2 is 82.6% (the details of the calculation are shown in Fig. S3†). The N_2 adsorption–desorption technique was used to characterize the surface area of the as-prepared sample. A typical type IV isotherm is distinctly observed (Fig. 2d). The specific surface area based on Brunauer–Emmett–Teller (BET) measurements is 209 $m^2\ g^{-1}$. Such a high specific area could offer more active sites and promote the electron/ion diffusion, leading to the enhanced performance.

To further analyze the composition and chemical state of the as-prepared CNT-MoS_2@MoO_2-C, X-ray photoelectron spectroscopy (XPS) was carried out. In Fig. 3a, Mo, S, O, C, and N can be distinctly detected in the XPS survey scan of the sample, indicating the existence of the above elements in the CNT-MoS_2@MoO_2-C composite. The high-resolution Mo spectrum is shown in Fig. 3b, the two peaks at 229.8 and 233.0 eV with a splitting energy of 3.2 eV can be attributed to Mo $3d_{3/2}$ and Mo $3d_{5/2}$ of MoS_2, respectively.[33] In addition, the other two peaks at the binding energy of 230.3 and 233.3 eV belong to MoO_2 with a splitting energy of 3.0 eV.[34] Mo^{6+} was also detected at around 236.6 eV, which is associated with the surface oxidation of Mo^{4+}

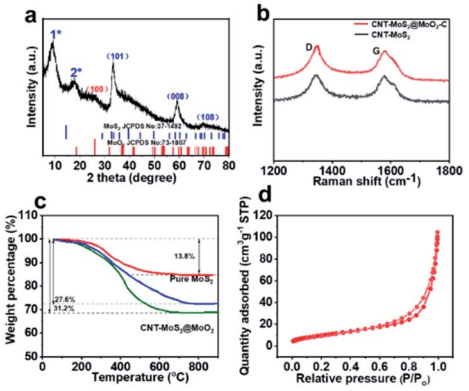

Fig. 2 (a) XRD pattern of CNT-MoS_2@MoO_2-C, (b) Raman profiles of CNT-MoS_2 and CNT-MoS_2@MoO_2-C, (c) TGA curves of pure MoS_2 and CNT-MoS_2@MoO_2-C, and (d) N_2 adsorption–desorption isotherm of CNT-MoS_2@MoO_2-C.

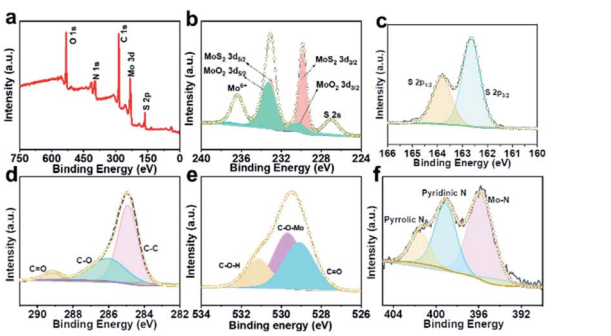

Fig. 3 (a) All survey, (b) Mo 3d, (c) S 2p, (d) C 1s, (e) O 1s, and (f) N high-resolution XPS spectra of CNT-MoS_2@MoO_2-C.

in air.[24] The small peak next to Mo $3d_{3/2}$ is assigned to S.[32] To further identify the surface electronic states of the as-prepared CNT-MoS_2@MoO_2-C, the Mo bonding states in CNT-MoS_2 and mixture of CNT-MoS_2 and MoO_2-C (CNT-MoS_2/MoO_2-C) are also detected. As shown in Fig. S4,† the Mo 3d spectrum of CNT-MoS_2 demonstrates typical Mo^{4+}–S peaks at binding energies of 229.3 and 232.5 eV. Compared with the spectrum of CNT-MoS_2, two additional peaks at 229.5 and 233.1 eV can be seen in the spectrum of CNT-MoS_2/MoO_2-C, which can be assigned to MoO_2 $3d_{3/2}$ and $3d_{5/2}$, suggesting the existence of MoO_2 in the mixture. Note that Mo^{4+}–S is still located at the same binding energy without any shift, which demonstrates that the mixture is physically blended without chemical bonds. In comparison, the two peaks of Mo 3d for CNT-MoS_2@MoO_2-C shifted to higher binding energy values, as a result of the coupling effect of MoS_2 and MoO_2 in the MoS_2/MoO_2 heterostructures.[22,35] These results agree with the generation of MoS_2/MoO_2 heterostructures as confirmed by XRD and TEM.

From the high-resolution S spectrum (Fig. 3c), there are two characteristic peaks at 162.5 and 163.7 eV, which are consistent with S $2p_{3/2}$ and S $2p_{1/2}$.[36] As shown in Fig. 3d, the peaks centered at 284.5, 286.2, and 289.3 eV could be assigned to the C–C, C–O, C=O bonds, respectively.[37] The O 1s peak (Fig. 3e) at 529.8 eV can be attributed to the Mo–O signal, which further confirms the existence of MoO_2 in the CNT-MoS_2@MoO_2-C composite. And the other peaks located at 529 and 531.5 eV can be attributed to the C=O and C–OH bond, respectively.[33] The N 1s spectrum is displayed in Fig. 3f, an apparent peak at 394.5 eV corresponds to the Mo–N bond, illustrating N doping and strong interaction in CNT-MoS_2@MoO_2-C. The other peaks at 398.3 and 401.7 eV are ascribed to pyridinic N and pyrrolic N, respectively, which are beneficial for the pseudocapacitive behavior, leading to fast reaction kinetics.[37] The XPS results further prove the formation of the as-predicted CNT-MoS_2@MoO_2-C structure.

The electrochemical performance of the CNT-MoS_2@MoO_2-C electrode was evaluated in 2032-type coin cells. The galvanostatic charge–discharge profiles of CNT-MoS_2@MoO_2-C at a current of 1 A g^{-1} are shown in Fig. 4a. The initial discharge and charge specific capacities are 809 and 607 mA h g^{-1}, corresponding to a high coulombic efficiency of 74% (*vs.* 56% for the CNT-MoS_2 composite shown in Fig. S5†). The increased ICE can be attributed to the MoO_2 nanocrystals anchored on 2D nanosheets, which could adsorb the polysulfides to improve the reversibility of MoS_2 at the interface.[38] Meanwhile, the dispersed MoO_2 and N-doped carbon would prevent restacking and agglomeration of MoS_2 during the charge/discharge process, offering more chemically active sites.[34] The initial irreversible capacity loss is mainly associated with the formation of solid electrolyte interphase (SEI) films.[39] From the second cycle, a capacity of 569 mA h g^{-1} can be achieved with an increased coulombic efficiency of 93%. After 50 cycles, the electrode maintained a highly reversible capacity of 563 mA h g^{-1} and an almost ~100% coulombic efficiency, which can be attributed to the stable interface. In order to further confirm the superiority of such an interface structure, the CNT-MoS_2 control was cycled at a current of 1 A g^{-1}. As shown in Fig. 4b, the CNT-MoS_2 electrode shows continued capacity decay and the capacity decreases to about 180 mA h g^{-1} after 800 cycles, which mainly results from the large volume expansion/contraction and uncontrolled aggregation of the active materials during charge/discharge processes. In contrast, CNT-MoS_2@MoO_2-C can maintain a much higher discharge capacity of 534 mA h g^{-1} with high cycling stability. The rate capabilities of the CNT-MoS_2@MoO_2-C electrode with various current rates from 0.2 to 10 A g^{-1} are demonstrated in Fig. 4c. The CNT-MoS_2@MoO_2-C electrode demonstrates an impressive rate performance, average capacities of 702, 598, 486, 453, 412 and 398 mA h g^{-1} were delivered at 0.2, 0.5, 1, 2, 5, and 10 A g^{-1}, respectively. In particular, a capacity of ~700 mA h g^{-1} could still be reached when the current was switched back to 0.2 A g^{-1}, after the deep charge/discharge cycles at a high current of 10 A g^{-1} for 10 cycles, which manifests the reversible and facile Na^+ insertion/extraction. As a comparison, the CNT-MoS_2 electrode exhibits inferior specific capacity, only 127 mA h g^{-1} at the current density of 10 A g^{-1}. Notably, the Na^+ storage of the CNT-MoS_2@MoO_2-C electrode is significantly enhanced compared with other reported MoS_2-based and MoO_2-based electrodes.[6,8,10,17,20,32,40] To further confirm the effect of the heterointerface on the Na^+ storage, the electrochemical performances of CNT-MoS_2/MoO_2-C (CNT-MoS_2 and MoO_2-C are physically blended by grinding without a heterojunction) are also evaluated. As shown in Fig. S6a,† the CNT-MoS_2/MoO_2-C electrode delivered a specific capacity of 200 mA h g^{-1} at a current of 1 A g^{-1} along with the continued capacity decay and the capacity decreased to ~150 mA h g^{-1} after 200 cycles. The rate capability of the mixture of CNT-MoS_2 and MoO_2-C is also investigated. From Fig. S6b,† only capacities of 72 and 46 mA h g^{-1} could be reached at currents of 5 and 10 A g^{-1}.

Long-term cycling performance is the key attribute for the application of SIBs. However, the large radius of Na^+ makes the charge transport difficult, and stress associated with volume change inevitably leads to structural collapse. Impressively, the as-prepared CNT-MoS_2@MoO_2-C electrode demonstrates excellent long-term cycling stability (Fig. 4d) even at the high current density of 5 A g^{-1}. The capacity can be well maintained with ~400 mA h g^{-1} after 5000 cycles with a stable coulombic efficiency of ~100%, which implies that the interface structure is highly reversible and stable. The structural stability of the

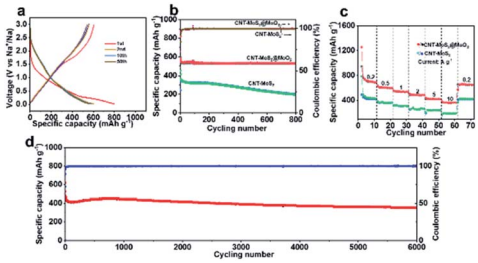

Fig. 4 (a) Charge–discharge profiles of the CNT-MoS_2@MoO_2-C electrode, (b) the cycling performance of CNT-MoS_2 and CNT-MoS_2@MoO_2-C electrodes at a current of 1 A g^{-1}, (c) rate capability of CNT-MoS_2 and CNT-MoS_2@MoO_2-C electrodes, and (d) long-term cycling performance at a current of 5 A g^{-1}.

CNT-MoS_2@MoO_2 electrode is evaluated by SEM and TEM after 100 cycles, as shown in Fig. S7.† It can be seen that the 1D morphology is well-retained and MoO_2 nanocrystals still uniformly dispersed on MoS_2 nanosheets, which illustrate the high structural stability.

To elucidate the charge transport mechanisms of Na^+ in the CNT-MoS_2@MoO_2-C electrode, the galvanostatic intermittent titration technique (GITT, shown in Fig. S8†) was performed. As shown in Fig. 5a, the GITT profile of CNT-MoS_2@MoO_2-C was obtained by applying a series of current pulses at 100 mA g^{-1} for 0.5 h followed by a 2 h relaxation process, and the potential change shown in the discharge curve corresponds to the Na^+ diffusion rate (D_{Na^+}). According to the equation[41]

$$D_{Na^+} = \frac{4}{\pi}\left(\frac{m_B V_M}{M_B A}\right)^2\left(\frac{\Delta E_s}{\Delta E_t}\right)^2\left(\tau \ll \frac{L^2}{D_{Na^+}}\right) \quad (1)$$

a series of D_{Na^+} at corresponding potentials can be quantified. The calculated D_{Na^+} of CNT-MoS_2@MoO_2-C is shown in Fig. 5b; the diffusivity of Na^+ is mostly constant across the voltage range. Moreover, the D_{Na^+} in CNT-MoS_2@MoO_2-C was higher than that of CNT-MoS_2 during the whole process, demonstrating enhanced diffusion kinetics by engineering the atomic heterointerface. The atomic heterointerface can effectively restrict the crystal grain growth and offer more crystal defects for fast ion diffusion.[15] Cyclic voltammetry (CV) was conducted to study the charge storage mechanism of CNT-MoS_2@MoO_2-C. Fig. 5c reveals the typical CV curves at a scan rate of 0.1 mV s^{-1} within the potential window of 0.01–3 V. In the first cycle, a broad reduction peak at 1.0–1.5 V in the cathodic process can be attributed to the intercalation of Na^+ into MoS_2 to form Na_x-MoS_2.[42] And the other broad peak at ~0.5 V could be associated with the formation of SEI film and the Na^+ intercalation in MoO_2.[24] The dominant peak at ~0.15 V is assigned to the conversion reaction of Mo and Na_2S.[8] In the following two cycles, the curves overlapped well, illustrating superior reversibility and stability of the CNT-MoS_2@MoO_2-C electrode during the charge/discharge process. Comparing with the reported MoS_2-based electrode, the CNT-MoS_2@MoO_2-C electrode shows enhanced reversibility, which can be attributed to the suppressed shuttle effect owing to the introduction of MoO_2. To further verify the effect of the MoO_2 nanocrystal in the CNT-MoS_2@MoO_2-C electrode, the CNT-MoS_2@MoO_2-C and CNT-MoS_2 electrodes were disassembled after several cycles at a current of 0.1 A g^{-1}. Digital images in Fig. S9† clearly show that the surface of the separator and counter electrode in the case of CNT-MoS_2@MoO_2-C was clearly without visible deposition. In contrast, yellow deposits were visible on the surface of the separator for the CNT-MoS_2 electrode. These results further demonstrate the effect of MoO_2, which can be combined with polysulfide in the atomic heterointerface and then suppresses the shuttle effect.[30] The charge storage mechanism of CNT-MoS_2@MoO_2-C is explored *via* CV at various scan rates. Fig. 5d shows the CV curves at scan rates from 0.1 to 2 mV s^{-1}, which show similar shape. It is assumed that the charge storage mechanism can be studied according to the relationship between the current (i) and scan rate (v):[43]

$$i = av^b \quad (2)$$

where a and b are the adjustable parameters, and the b-value can be calculated from the slopes of log(v)–log(i) plots. Specifically, the charge storage is controlled by diffusion when b is 0.5, whereas $b = 1$ indicates that the capacitive behavior dominates the whole process. Fig. 5e illustrates a series of b values at different potentials during the cathodic process, and the inset is the plot of log(v)–log(i). The majority b values are higher than 0.8, which suggest that the capacitive behavior plays a dominant role in the charge storage, promoting fast kinetics. The capacitive contribution to the total charge storage at specified scan rate can be quantitatively analyzed according to the following equation:[43]

$$i = k_1 v + k_2 v^{\frac{1}{2}} \quad (3)$$

where $k_1 v$ represents the capacitive effect, which can be obtained through calculating k_1. As demonstrated in Fig. 5f, the capacitive contribution for the CNT-MoS_2@MoO_2-C electrode at a scan rate of 0.5 mV s^{-1} (shaded area) is ~84% of the whole charge storage.

As expected, the CNT-MoS_2@MoO_2-C structure with well-known characteristics have shown compelling Na^+ storage performance, which mainly benefits from the following: (1) the expanded interlayer space can offer more active sites for adsorbing Na^+ and promote fast insertion/extraction of Na^+, resulting in fast reaction kinetics; (2) the shuttle effects of intermediate polysulfides generated through the conversion reaction can be well suppressed by the introduction of MoO_2, which acts as an adsorbent to immobilize polysulfides, promoting the reversibility of the reaction. Moreover, the growth of MoO_2 on the MoS_2 surface can avoid the aggregation and restacking of 2D MoS_2 during the charge/discharge process, ensuring the exposure of the active sites; (3) the CNTs and highly conductive N-doped carbon as the sandwiched layer can tightly integrate the MoS_2/MoO_2, which not only increases the charge transfer but also buffers the volume expansion during the charge/discharge process, contributing to the structural stability and cycling reversibility. The electrochemical

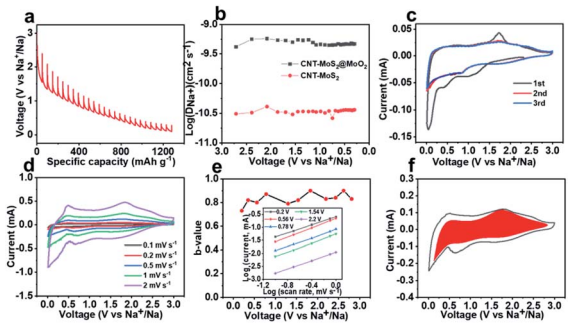

Fig. 5 (a) GITT profile of the CNT-MoS_2@MoO_2-C electrode, (b) the corresponding Na^+ diffusion coefficient at different potentials, (c) CV curves at a scan rate of 0.1 mV s^{-1}, (d) CV curves at different scan rates ranging from 0.1 to 2 mV s^{-1}, (e) the calculated b values at different potentials, and (f) the capacitive behavior distinguished from the CV curves at a scan rate of 0.5 mV s^{-1}.

impedance spectra (EIS) were recorded to better understand the kinetics of the CNT-MoS_2@MoO_2-C, CNT-MoS_2, and MoO_2-C electrodes, the results were fitted with an equivalent electrical circuit (Fig. S10†). The CNT-MoS_2@MoO_2-C electrode demonstrates a lower charge transfer resistance than the CNT-MoS_2 (869 Ω) and MoO_2-C (567 Ω), which can be attributed to the rapid electron transfer effects of CNTs and N-doped carbon in the sandwich-type structure;[44] (4) the enhanced pseudocapacitance with the hierarchical nanostructure can effectively facilitate fast kinetics in charge transfer and transport.

In addition to the aforementioned merits, the enhancement in the capacities of the composite electrodes has often been ascribed to an ambiguous "synergetic effect" without further clarification or discussion on the exact roles of the interface. In this work, the CNT-MoS_2@MoO_2-C electrode features distinct differences from previously reported composite materials in terms of the nanoscale heterointerface, which could maximize the Na^+ storage and transport. To further understand the effect of such an interesting atomic heterointerface on the Na^+ storage behavior, DFT calculations were carried out. In this structure, MoS_2 is a typical p-type semiconductor with a band gap of 1.89 eV,[45] while MoO_2 works as a wide band gap n-type semiconductor (3.85 eV).[46] Therefore, the built-in electric field could be present at the heterointerface when the MoS_2/MoO_2 p–n heterojunction is formed. The electrostatic potentials of MoS_2 and MoO_2 are examined, respectively, to further reveal the electron distributions in the heterointerface. As shown in Fig. 6a and b, MoS_2 demonstrates a lower Fermi level than MoO_2. Once the heterointerface is formed, these Fermi levels tend to align. The internal electric field can promote the accumulation of negative charges on the MoS_2 surface and positive charges on the MoO_2 surface, leading to a charge transport pathway from MoO_2 to MoS_2. Under this electric field, Na^+ can strongly adsorb on the MoS_2 surface due to the electrostatic attraction between Na^+ and the accumulated negative charge. As shown in Fig. 6c, the Na^+ diffusion barriers in the MoO_2, MoS_2 and MoS_2/MoO_2 interface were also calculated. From the calculated results, the CNT-MoS_2@MoO_2-C interface demonstrated a lower diffusion barrier (0.24 eV), which is lower than that of MoS_2 (0.33 eV) and MoO_2 (0.41 eV), suggesting that the

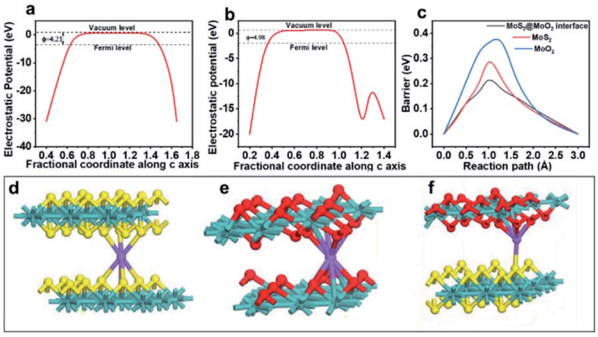

Fig. 6 (a) MoS_2 and (b) MoO_2 electrostatic potentials, (c) the diffusion barrier of MoO_2, MoS_2, and MoS_2/MoO_2 interface, and Na adsorption on various systems (d) MoS_2 interface, (e) MoO_2 interface and (f) MoS_2/MoO_2 heterointerface.

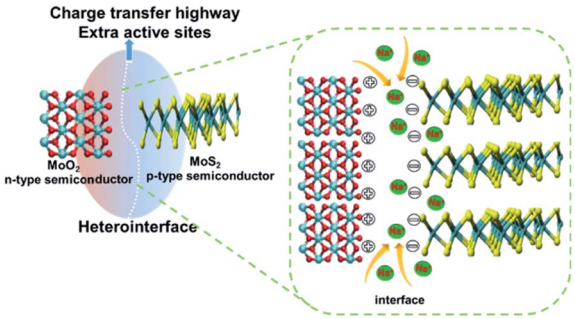

Scheme 2 Summary of the enhanced electrochemical performance of the MoS_2/MoS_2 heterointerface.

Na^+ diffusion at the interface is more favorable for faster kinetics. In the LIBs, Jamink and Maier have proposed a "job-sharing" mechanism in which the Li^+ can be stored in the solid/solid interface. This well explains the extra Li storage at the interface. In order to verify if the enhancement of Na^+ storage can be attributed to the interfacial effect in our structure, the Na^+ storage capability of the heterointerface is investigated systematically. According to the calculated results, Na^+ preferentially adsorbs on top of the Mo site with the $E_{ad} = 2.14$ eV, which shows stronger binding ability compared to S ($E_{ad} = 189$ eV). In this configuration, Na^+ lies on the Mo site, and combines with the 3 nearest S atoms in the form of Na–Mo and Na–S bonds, respectively (Fig. 6d). Similarly, in the MoO_2 structure, the most stable position is Na^+ adsorption on the Mo site with $E_{ad} = 1.98$ eV. The interface of MoS_2/MoO_2 is engineered by the (002) plane of MoS_2 and (100) plane of MoO_2 according to the XRD results. Compared with the single MoS_2 and MoO_2, the corresponding adsorption energies of the MoS_2/MoO_2 interface demonstrate significant enhancement, giving an $E_{ad} = 2.89$ eV, in which Na aligns with the Mo site of MoS_2. The enhancement of the E_{ad} can be reasonably attributed to the synergetic effect of introducing MoO_2 to construct the MoS_2/MoO_2 interface for additional adsorption sites for Na^+. Based on the above calculated results, a reasonable mechanism is proposed to explain the enhancement of Na^+ storage, as shown in Scheme 2. In our designed interface, MoS_2 and MoO_2 act as p-type and n-type semiconductors, respectively. Therefore, the built-in electric field could have formed when the heterointerface was constructed, which could accelerate the charge separation and migration efficiencies, promoting fast reaction kinetics. Moreover, the low barrier of interface could reduce the impedance for charge storage further to improve rate capability. Besides providing faster charger-transfer kinetics, the heterointerface could offer extra sites for Na storage.

Conclusions

In conclusion, we have designed and synthesized a robust 3D nanoarchitecture involving a N-doped carbon layer anchoring MoS_2 nanosheets decorated with MoO_2 nanocrystals directly on the CNT surface. The engineered nano-heterointerface between MoS_2 nanosheets and MoO_2 nanocrystals can maximize the

interfacial synergistic effect to reduce the ion transfer barrier, promote faster reaction kinetics, and provide more active sites. Moreover, our nanocomposite with highly conductive CNTs, protecting carbon layers, and uniform distribution of nanocrystals could further promote the pseudocapacitive behavior and maintain the stability of the whole composite during the charge/discharge cycles. These characteristics provide the CNT-MoS_2@MoO_2-C electrode with high energy density as well as high cycling stability when used as the negative electrode for SIBs, which are superior to all reported Mo-based negative electrodes in SIBs. Notably, it delivered an excellent rate capacity of 375 mA h g^{-1} at 10 A g^{-1} and ultra-long cycle life over 6000 cycles at 5 A g^{-1}. Based on the insights on atomic heterointerfaces, the present work could open a new pathway to the rational design and fabrication of other hybrid materials for rechargeable batteries.

Conflicts of interest

There are no conflicts to declare.

Acknowledgements

C. Ma and H. Xiong acknowledge support from the National Science Foundation under Grant No. DMR-1454984. This work was also supported by the National Basic Research Program of China (2014CB239700), the National Natural Science Foundation of China (21905160, 21776175), and the Natural Science Foundation of Shanghai (19ZR1424600).

Notes and references

1 K. Matsumoto, J. Hwang, S. Kaushik, C.-Y. Chen and R. Hagiwara, *Energy Environ. Sci.*, 2019, **12**, 3247–3287.
2 Y. Liu, C. Yang, Q. Zhang and M. Liu, *Energy Storage Mater.*, 2019, **22**, 66–95.
3 B. Sun, P. Xiong, U. Maitra, D. Langsdorf, K. Yan, C. Wang, J. Janek, D. Schroeder and G. Wang, *Adv. Mater.*, 2019, **10**, 1903891.
4 Y. Wang, Y. Wang, Y.-X. Wang, X. Feng, W. Chen, X. Ai, H. Yang and Y. Cao, *Chem*, 2019, **5**, 2547–2570.
5 C. Zhao, L. Liu, Y. Lu, M. Wagemaker, L. Chen and Y.-S. Hu, *Angew. Chem., Int. Ed.*, 2019, **58**, 17026–17032.
6 W. Ye, F. Wu, N. Shi, H. Zhou, Q. Chi, W. Chen, S. Du, P. Gao, H. Li and S. Xiong, *Small*, 2019, **10**, 1906607.
7 H. Wu, X. Zhang, Q. Wu, Y. Han, X. Wu, P. Ji, M. Zhou, G. Diao and M. Chen, *Chem. Commun.*, 2020, **56**, 141–144.
8 Y. Li, R. Zhang, W. Zhou, X. Wu, H. Zhang and J. Zhang, *ACS Nano*, 2019, **13**, 5533–5540.
9 L. Xing, Q. Yu, B. Jiang, J. Chu, C.-Y. Lao, M. Wang, K. Han, Z. Liu, Y. Bao and W. Wang, *J. Mater. Chem. A*, 2019, **7**, 5760–5768.
10 Q. Pan, Q. Zhang, F. Zheng, Y. Liu, Y. Li, X. Ou, X. Xiong, C. Yang and M. Liu, *ACS Nano*, 2018, **12**, 12578–12586.
11 Z. Li, K. Jiang, F. Khan, A. Goswami, J. Liu, A. Passian and T. Thundat, *Sci. Adv.*, 2019, **5**, 2820.
12 S. Lu, T. Zhu, H. Wu, Y. Wang, J. Li, A. Abdelkader, K. Xi, W. Wang, Y. Li, S. Ding, G. Gao and R. V. Kumar, *Nano Energy*, 2019, **59**, 762–772.
13 J. Feng, Y. Dong, Y. Yan, W. Zhao, T. Yang, J. Zheng, Z. Li and M. Wu, *Chem. Eng. J.*, 2019, **373**, 565–571.
14 Z. Li, Y. Dong, J. Feng, T. Xu, H. Ren, C. Gao, Y. Li, M. Cheng, W. Wu and M. Wu, *ACS Nano*, 2019, **13**, 9227–9236.
15 H. Jiang, D. Ren, H. Wang, Y. Hu, S. Guo, H. Yuan, P. Hu, L. Zhang and C. Li, *Adv. Mater.*, 2015, **27**, 3687–3695.
16 Y. N. Ko, S. H. Choi, S. B. Park and Y. C. Kang, *Nanoscale*, 2014, **6**, 10511–10515.
17 W. Ren, H. Zhang, C. Guan and C. Cheng, *Adv. Funct. Mater.*, 2017, **27**, 1702116.
18 C. Zhao, C. Yu, B. Qiu, S. Zhou, M. Zhang, H. Huang, B. Wang, J. Zhao, X. Sun and J. Qiu, *Adv. Mater.*, 2018, **30**, 1702448.
19 J. Duan, G. Qin, L. Min, Y. Yang and C. Wang, *ACS Appl. Mater. Interfaces*, 2018, **10**, 38084–38092.
20 K. Ma, H. Jiang, Y. Hu and C. Li, *Adv. Funct. Mater.*, 2018, **28**, 1804306.
21 Y. Li, H. Wang, L. Wang, R. Wang, B. He, Y. Gong and X. Hu, *Energy Storage Mater.*, 2019, **23**, 95–104.
22 Y. Zheng, T. Zhou, C. Zhang, J. Mao, H. Liu and Z. Guo, *Angew. Chem., Int. Ed.*, 2016, **55**, 3408–3413.
23 L. Fang, Z. Lan, W. Guan, P. Zhou, N. Bahlawane, W. Sun, Y. Lu, C. Liang, M. Yan and Y. Jiang, *Energy Storage Mater.*, 2019, **18**, 107–113.
24 C. Ma, X. Li, C. Deng, Y.-Y. Hu, S. Lee, X.-Z. Liao, Y.-S. He, Z.-F. Ma and H. Xiong, *ACS Nano*, 2019, **13**, 2664.
25 Y.-Q. Wu, H.-X. Yang, Y. Yang, H. Pu, W.-J. Meng, R.-Z. Gao and D.-L. Zhao, *Small*, 2019, **15**, 1903873.
26 Y. Liu, K. Ai and L. Lu, *Chem. Rev.*, 2014, **114**, 5057–5115.
27 E. Xu, Y. Zhang, H. Wang, Z. Zhu, J. Quan, Y. Chang, P. Li, D. Yu and Y. Jiang, *Chem. Eng. J.*, 2020, **385**, 123839.
28 D. Ren, Y. Hu, H. Jiang, Z. Deng, P. Saha, H. Jiang and C. Li, *ACS Sustainable Chem. Eng.*, 2016, **4**, 1148–1153.
29 S. Zhang, B. V. R. Chowdari, Z. Wen, J. Jin and J. Yang, *ACS Nano*, 2015, **9**, 12464–12472.
30 X. Xie, T. Makaryan, M. Zhao, K. L. Van Aken, Y. Gogotsi and G. Wang, *Adv. Energy Mater.*, 2016, **6**, 1502161.
31 S. Wang, Z. Zhang, Y. Yang and Z. Tang, *ACS Appl. Mater. Interfaces*, 2017, **9**, 23741–23747.
32 Z. Chen, D. Yin and M. Zhang, *Small*, 2018, **14**, 1703818.
33 Y. Liu, Y. Xiao, F. Liu, P. Han and G. Qin, *J. Mater. Chem. A*, 2019, **7**, 26818–26828.
34 X. Zhao, H.-E. Wang, Y. Yang, Z. G. Neale, R. C. Masse, J. Cao, W. Cai, J. Sui and G. Cao, *Energy Storage Mater.*, 2018, **12**, 241–251.
35 K. Zhu, X. Wang, J. Liu, S. Lo, H. Wang, L. Yang, S. Liu and T. Xie, *ACS Sustainable Chem. Eng.*, 2017, **5**, 8025–8034.
36 X.-Y. Yu, H. Hu, Y. Wang, H. Chen and X. W. Lou, *Angew. Chem., Int. Ed.*, 2015, **54**, 7395–7398.
37 C. Ma, C. Deng, X. Liao, Y. He, Z. Ma and H. Xiong, *ACS Appl. Mater. Interfaces*, 2018, **10**, 36969–36975.
38 R. Li, X. Zhou, H. Shen, M. Yang and C. Li, *ACS Nano*, 2019, **13**, 10049–10061.

39 Z. Zhu, S. Xi, L. Miao, Y. Tang, Y. Zeng, H. Xia, Z. Lv, W. Zhang, X. Ge, H. Zhang, J. Wei, S. Cao, J. Chen, Y. Du and X. Chen, *Adv. Funct. Mater.*, 2019, **29**, 1904843.
40 B. Chen, H. Lu, J. Zhou, Y. Chao and S. Z. Qiao, *Adv. Energy Mater.*, 2018, **26**, 1702909.
41 T.-T. Shan, S. Xin, Y. You, H.-P. Cong, S.-H. Yu and A. Manthiram, *Angew. Chem., Int. Ed.*, 2016, **55**, 12783–12788.
42 M. Hou, Y. Qiu, G. Yan, J. Wang, D. Zhan, X. Liu, J. Gao and L. Lai, *Nano Energy*, 2019, **62**, 299–309.
43 J. Wang, J. Polleux, J. Lim and B. Dunn, *J. Phys. Chem. C*, 2007, **111**, 14925–14931.
44 N. Zheng, G. Jiang, X. Chen, J. Mao, Y. Zhou and Y. Li, *J. Mater. Chem. A*, 2019, **7**, 9305–9315.
45 S. Chuang, C. Battaglia, A. Azcatl, S. McDonnell, J. S. Kang, X. Yin, M. Tosun, R. Kapadia, H. Fang, R. M. Wallace and A. Javey, *Nano Lett.*, 2014, **14**, 1337–1342.
46 D. O. Scanlon, G. W. Watson, D. J. Payne, G. R. Atkinson, R. G. Egdell and D. S. L. Law, *J. Phys. Chem. C*, 2010, **114**, 4636–4645.

